Deformation Mechanisms Rationalisation to Design for Creep Resistance in Polycrystalline Ni-Based Superalloys

D. BARBA, A. EGAN, S. UTADA, Y. GONG, Y.T. TANG, V. MAZANOVA, M.J. MILLS, and R.C. REED

Creep strength in polycrystalline Ni-based superalloys is influenced by the formation of a rich variety of planar faults forming within the strengthening γ' phase. The lengthening and thickening rate of these faults – and therefore the creep rate – depends on an intriguing combination of dislocation interactions at the γ-γ' interface and diffusional processes of the alloying elements at the core of the fault tip. The effect of alloy composition on this process is not fully understood. In this work we use correlative high resolution transmission electron microscopy and energy-dispersive X-ray spectroscopy to study the deformation faults in two different Ni-based superalloys with carefully designed ratios of disordering-to-ordering-promoting elements (Co-Cr against Nb-Ta-Ti). The results show that the additions of ordering-promoting elements reduce the diffusional processes required for the faults to lengthen and thicken thus reducing the creep rates found for the higher Nb-Ta-Ti alloy. These insights provide a path to follow in the design of improved grades of creep-resistant polycrystalline alloys beyond 700 °C.

I. INTRODUCTION

THE mid-temperature creep strength of Ni-based superalloys has been recently found to be influenced by segregation processes associated with shearing of the γ' phase by planar faults.[1–9] This is specifically the case for polycrystalline grade superalloys in which this temperature region is within their critical in-service regime.[10,11] The segregation of γ stabiliser elements while the complex fault is growing within the γ' has been found to enhance their lengthening rate. This is due to the fact that these elements greatly reduce the energy associated with the fault by stabilising a locally disordered structure.[12–18] Some alloys seem to be more prone to segregation-assisted fault formation than others, presenting in some cases extensive deformation twins thickened from embryonic complex extrinsic stacking faults (CESF). In that case the creep performance of the alloy deteriorates abruptly.[19–21] The underlying reasons by which some alloys are more sensitive than others to this weakening mechanism is still controversial.

More recently, some authors have found a corollary to this segregation effect.[2,4,5,22,23] They found that segregation of non-γ stabiliser elements like Ti, Nb, or Ta can produce a completely different effect on the creep performance.[2,5,7,23,24] The creep life of these alloys were found to be superior to the ones in which Co-Cr segregated faults are found. The rationalisation behind this is the formation of other phases like η or χ which presumably present slower formation kinetics. Some authors have used atomistic simulations to rationalise the effect of these chemical variations along the faults on the stacking fault energies and therefore shearing resistance of the alloys[25,26] However, the effect of the alloy composition on governing the type of segregation is still not fully understood and further experimental observations are needed. In this regard further systematic experimentation is needed to understand the

D. BARBA is with the Department of Materials, University of Oxford, Parks Road, Oxford OX13PH, U.K. and also with the E.T.S. Ingeniería Aeronáutica y del Espacio, Universidad Politécnica de Madrid, Plaza Cardenal Cisneros, 3, 28040 Madrid, Spain. Contact e-mail: daniel.barba@upm.es A. EGAN, V. MAZANOVA and M.J. MILLS are with the Center for Electron Microscopy and Analysis, The Ohio State University, Columbus, OH 43212 and also with the Department of Materials Science and Engineering, The Ohio State University, Columbus, OH 43210. S. UTADA and Y.T. TANG are with the Department of Materials, University of Oxford. Y. GONG is with the Department of Materials, University of Oxford and also with the Max-Planck-Institut für Eisenforschung, Düsseldorf 40237, Germany. R.C. REED is with the Department of Materials, University of Oxford, and also with the Department of Engineering Science, University of Oxford, Parks Road, Oxford OX13PJ, U.K. Manuscript submitted July 31, 2022; accepted November 25, 2022.
Article published online January 15, 2023

chemistry dependence of the fault extension kinetics and ultimately how this affects the creep performance of the macroscopic material. Consequently, new nano- and micro-mechanical interpretations need to be advanced, for scientific benefit and technological effect.

This is the focus of this work: understanding the underlying mechanisms behind the effect of alloy chemistry on the creep performance of Ni-based superalloys from a deformation mechanistic point of view. To this purpose, two different Ni-superalloy systems with different ratios of Co-Cr to Nb-Ti-Ta have been selected. First, results on the creep performance of both alloys are introduced. Then, the different deformation mechanisms activated for the two alloys are studied by means of atomic resolution transmission microscopy and related to their creep performance. Third, the segregation phenomenon associated with the deformation mechanisms is studied by means of atomic resolution energy-dispersive X-ray (EDX) composition analysis. Finally, the insights are introduced in a diffusion-based mathematical modelling of fault formation in Ni-based superalloys which provides a complete understanding of the link between alloy composition → deformation mechanism → creep performance.

II. EXPERIMENTAL METHODS

A. *Materials*

Two different polycrystalline Ni-based superalloys were studied. These were produced using industry-standard powder processing methods, following Hisazawa *et al.*[27] Their compositions are presented in Table I. These compositions are selected to carefully study the effect of disorder promoting elements like Co + Cr (stabilisers of disordered phase γ) and order promoting elements like Nb + Ta + Ti (stabilisers of ordered phases like γ, η or χ). This shift in chemistry can be observed in Figure 1 where the amount of Co-Cr against Nb-Ta-Ti is compared for the nominal alloy composition and specifically for the γ'-phase (predicted from Thermocalc calculations using TTNI8 database). As indicated, for both the nominal and the γ' composition Alloy A has a higher amount of disorder promoting elements and lower levels of ordering elements, in contrary to Alloy B. This difference is more acute for the γ'-phase composition than for the nominal alloy composition. Focus is put on the γ' composition as it controls the growth rate of the faults.[1]

In order to focus on the effect of alloy composition on creep performance and reduce the influence of other variables, the microstructures of the two alloys were homogenised to approximately the same grain size and γ' distribution. For this purpose the alloys were solution treated at 1210 °C for 2 hours, followed by ageing for 2 hours at 830 °C. The grain size and γ' size distributions were measured using scanning electron microscopy (SEM) imaging in combination with image analysis. The image analysis was performed using an in-house software suite for microstructural analysis. To address the homogeneity of the microstructure, the analysis of each microstructural feature was extended to a total of 5 different images from regions of each alloy. For the measurement of the γ' fractions two different magnifications were used: lower magnification (×10,000) to extract the secondary γ' distribution and higher magnification to extract the tertiary γ' fraction (×40,000). The number of particles analysed in each image ranges between 668 and 913 for secondary gamma prime. For measuring the grain size distribution a magnification of ×270 was used. The number of grains analysed for each image ranges from 86 to 123 grains for each image. The results are presented in Figure 2. The average grain size, secondary and tertiary γ' size are presented in Table II along with the deviation between the different regions analysed. The results show similar grain size distribution with less than 10 pct deviation in the mean grain size. Similar results are observed for the secondary and tertiary γ' sizes. These results assure the simplification of the problem as the microstructural influence on creep performance and operative deformation mechanisms is eliminated, leaving alloy composition to play a role.

B. *Creep Testing*

Cylindrical compression creep test pieces were extracted from heat treated alloy bars with a diameter and height of 5 mm using electrical discharge machining (EDM). Monotonic creep compression tests were performed at 760 °C under an applied compressive load of 552 MPa, consistent with typical service conditions for these alloys.[19,28] Testing was conducted in an Instron servohydraulic testing machine equipped with furnace heating allowing digital image correlation (DIC) for non-contact strain measurement, as shown in Figure 3-(1). Creep tests were stopped at 22.5 hours to study the operative deformation mechanisms at that time.

C. *STEM-EDX Analysis*

Post-mortem examination prior to scanning transmission electron microscopy (STEM) and electron-backscattered (EBSD) analysis was carried out in order to identify suitable and consistent deformation grains between the two alloys to focus the TEM analysis. An overview of the combined TEM and EBSD analysis is presented in Figure 3-(2–4). The samples were prepared by grinding and polishing finished with colloidal silica. For both alloys, grains oriented along the ⟨001⟩ axis along the compression direction of the specimen were selected. This preliminary study was performed using a JEOL 6500F field emission gun scanning electron microscope (FEG-SEM) using an accelerating voltage of 10 kV and probe current of 300 pA. STEM samples were extracted from these grains normal to ⟨011⟩ crystal orientation using an FEI Helios Nanolab Dualbeam 600 focused ion beam (FIB), see Figure 3-(3). This assures planar faults are viewed edge-on using high angle annular dark field (HAADF) zone axis imaging. Samples were thinned at 5 kV and then further cleaned using a Fischione Nanomill.

Energy-dispersive X-ray analysis (EDX) and STEM of the samples was performed on an probe-corrected Themis Z at 200kV with a Super-X detector utilizing the Thermofisher Velox software. Integrated line scans were conducted and quantified through Cliff-Lorimer analysis[29] using experimental K_α energies for Ni, Co, Al, Cr and Ti. L_α was used for the case of Mo. The Cu specimen holder signal was avoided using the M_α lines for Ta and W since the L_α Ta and W peaks corresponded too closely to a Cu peak to be accurately considered. Deconvolution for the W and Ta M_α peaks, as well as background subtraction, was used to reduce the influence of Bremsstrahlung. With the purpose of comparing the role of microtwinning mechanism in both alloys, an estimation of the twin population has been performed. This analysis has been performed for each alloy in two different regions of the TEM sample to avoid localness. Two quantities has been estimated; the total length of twins per unit area and the average twin thickness. This last quantity has been estimated in high-magnification TEM micrographs ($\times100$k) by measuring the thickness of 15 different twin bands in Alloy A and 12 twin bands in Alloy B.

Table I. Compositions of the Two Ni-Based Superalloys Under Study

Composition (at. pct)	Cr	Co	W	Al	Ti	Ta	Nb
Alloy A	18.7	18.3	0.9	8.0	3.6	0.6	0.4
Alloy B	16.0	14.0	1.0	7.0	3.5	1.0	1.0

III. RESULTS

The creep strain curves for both alloys are presented in Figure 4. Summary results extracted from these curves are shown in Figure 5. For both alloys, primary and secondary creep stages can be identified. Alloy B presents a better creep performance than Alloy A. The steady-state creep rate of Alloy B is 20 pct lower than the one observed for Alloy A. Similar results are extracted in terms of the creep strain experienced by both alloys at the end of the 22.5h interrupted test (41 pct lower for Alloy B than for alloy A) and for the time required to reach 1 pct of creep strain (almost five more times for Alloy B than for Alloy A).

In order to rationalise the creep performance of both alloys, the operative deformation mechanisms were studied using STEM analysis of samples extracted from the interrupted test samples. The STEM micrographs for both alloys are presented in Figure 6 including overall images of the microstructure and more magnified micrographs for detailed analysis of the operative mechanism. For both alloys, complex dislocation structures can be found specifically concentrated at the γ-channels. The concentration of these dislocation bundles seems higher for Alloy B, even when the final creep strain is lower. This is likely to be caused by a superior γ' penetration resistance for dislocations when compared to Alloy A. Another major difference between the deformation structures is that the microstructure of Alloy A is densely populated by extensive faults. Further examination identified them as microtwins and extrinsic and intrinsic stacking faults – either complex (CESF/CISF) or superlattice (SESF-SISF). These faults extend through both γ and γ' phases. In contrast, the microstructure of Alloy B presents mostly faults of an
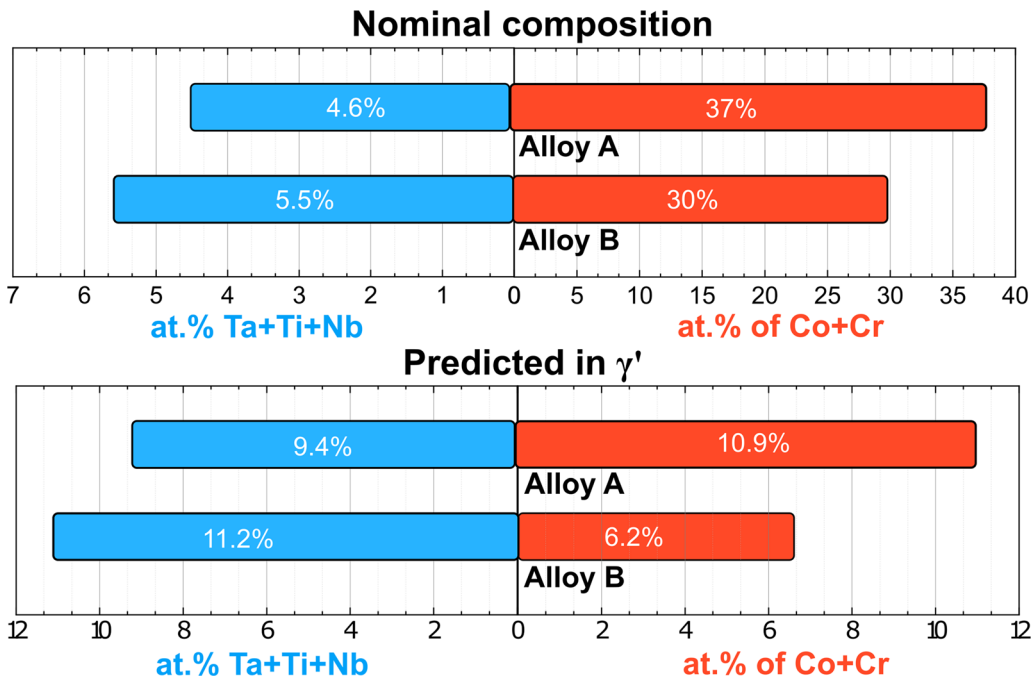

Fig. 1—Top: Nominal amount of at. pct Co + Cr and Ta + Ti + Nb of both alloys; Bottom: Co + Cr and Ta + Ti + Nb atomic percentage estimated for the γ' phase. Prediction computed from Thermocalc simulation using TTNI8 database.
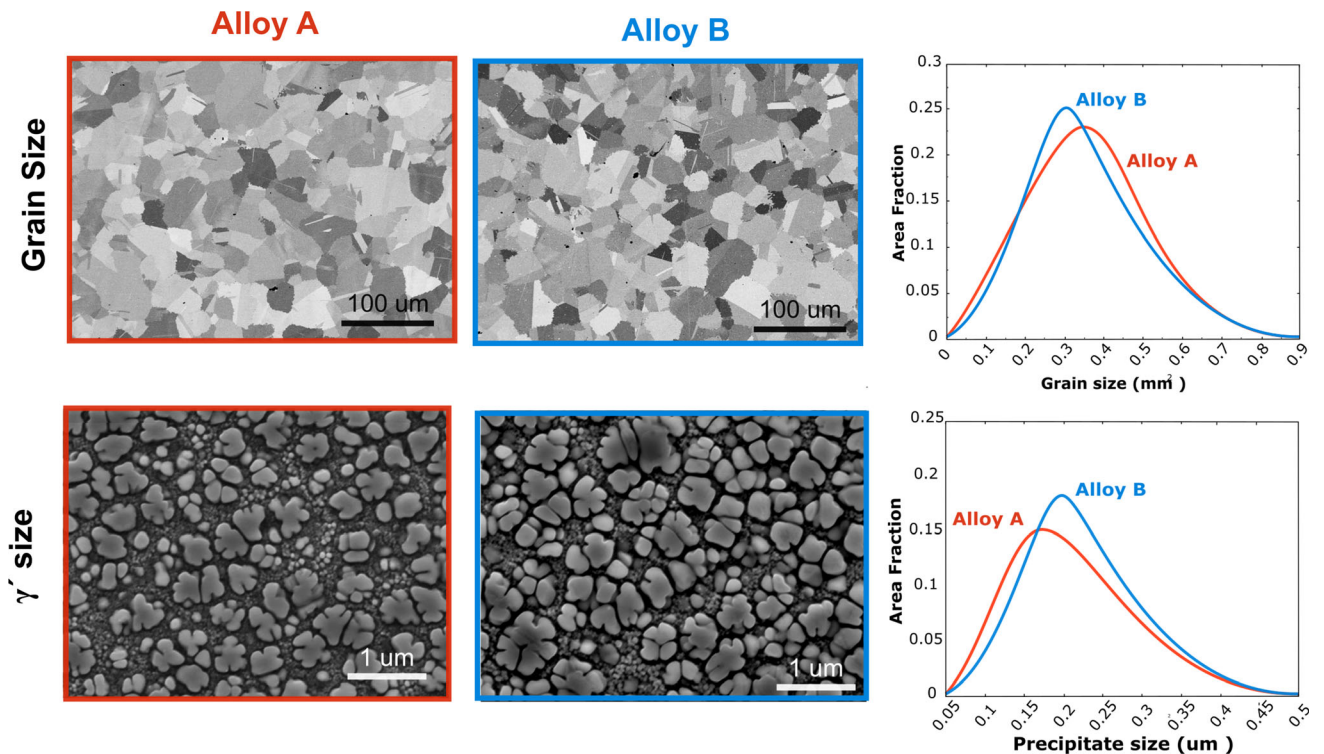
Fig. 2—Top: SEM images of the grain microstructure for both alloys and grain size distribution extracted from image analysis. Bottom: Microstructural images of the γ' precipitates for both alloys and secondary γ' size distribution extracted from image analysis.

isolated nature (later identified as SESFs/CESFs). Although a reduced number microtwins were observed when high-magnification was reached, the amount and thickness of them is significantly lower than for Alloy A. To confirm this point, quantitative estimations of the total twin length per unit area and average twin thickness has been performed. The results are presented in Table III. The following stats outcome by observing the ratios of the measured quantities between Alloy A and Alloy B: the total length of twins is 2.8 longer in Alloy A than in Alloy B (twins are more extensive in Alloy A) and the twins are in average 4.1 times thicker in Alloy A than in Alloy B.

Based on these observations, a clear change of mechanism is prevalent: a transition from mature and extensive thick faults (Alloy A) to a more incipient embryonic type of faults (Alloy B). This observation is in accordance with the creep performance of each alloy, as thicker and extensive faults (especially microtwins) are known to accelerate creep deformation.

For each alloy, representative faulted structures were analysed using combined STEM and EDX chemical analysis. Atomic resolution STEM was used to identify the type of faults (CISF-SISFs, SESFs/CESFs, microtwins or anti-phase boundaries). Chemical EDX analysis was used to identify the segregation processes occurring for each alloy. It is important to note that the segregation and diffusional processes detailed in this work are always referred to the shearing process within the γ'-precipitates. This analysis is presented next.

A. Faults in Alloy A

Two different faults representative of the active deformation mechanisms found in Alloy A are considered here: a bilayer SESF/CESF and a microtwin (23 layer thickness).

The HAADF-STEM image in the $\langle 011 \rangle$ zone axis of a **SESF/CESF** within the γ' phase is presented in Figure 7. The present analysis cannot distinguish between complex or superlattice faults (further atomic resolution EDX analysis is needed). Higher intensity is observed at the fault line which can be connected with elemental segregation of heavy elements. This is confirmed by the EDX analysis presented in the same figure. Intensive segregation of Cr and Co has occurred at the fault line. Cr double its value at the fault when compared with the surrounding γ' composition. Co levels are around 50 pct higher at the fault line than in the parent phase. In contrast, the Al levels are lower. Ta concentration shows some increase at the fault, but the results are not conclusive as segregation fluctuations are of the same order as the noise. Similar results were found in other studies on Ni-based superalloys, e.g., Ashton et al.[13] and Barba et al.[22]

The STEM and chemical analysis of a representative **microtwin** (23 layer thickness) is presented in Figure 8. This microtwin is representative of the fault population observed in the rest of the sample. Again, higher HAADF intensity levels are presented at the microtwin interfaces. The concentration profiles presented in this figure confirm the segregation and depletion of elements concentrated at the twin boundaries. Elemental

Table II. Microstructural Statistics for the 2 Alloys Extracted from Image Analysis, See Fig. 2

	Alloy A	Alloy B
Average Grain Size (mm^2)	0.328 ± 0.012	0.347 ± 0.014
Average Secondary γ' Size (μm^2)	0.192 ± 0.010	0.212 ± 0.016
Secondary γ' Fraction (percent)	68.5 ± 4.2	71.1 ± 3.9
Tertiary γ' Fraction (Percent)	2.31 ± 0.23	2.21 ± 0.31

Average sizes and fractions for a total of 5 images are presented along with their errors.
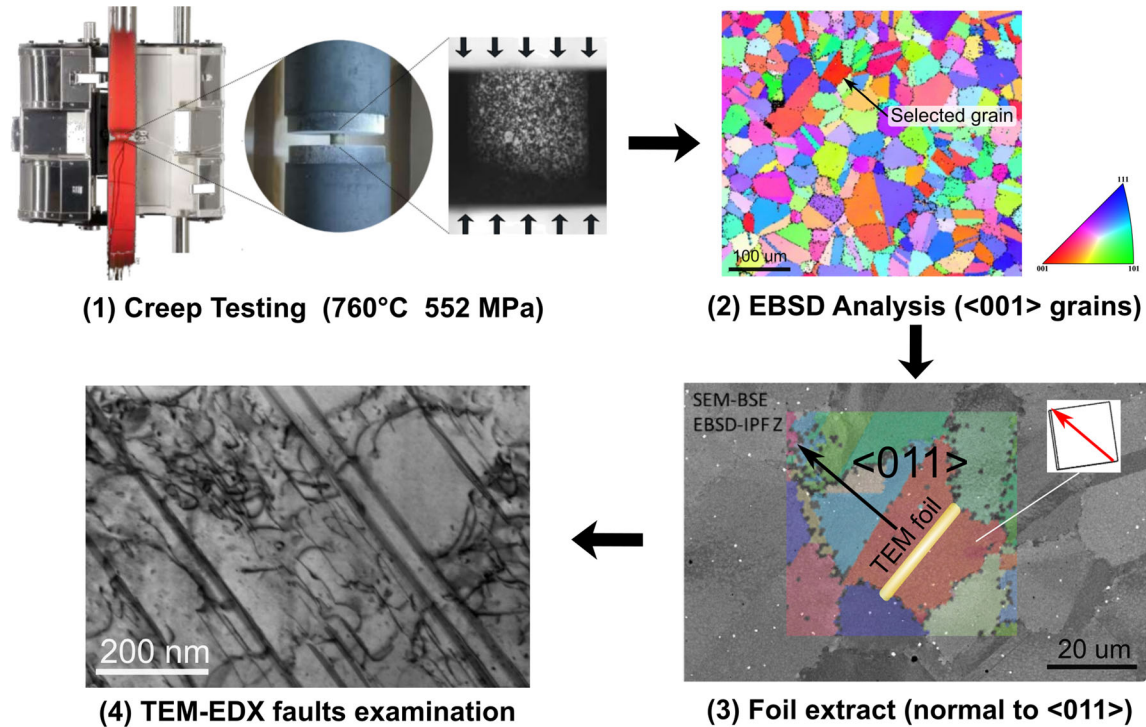
Fig. 3—Overview of the material analysis: (1) Creep testing of both alloys at 760 °C and 552MPa for 22.5h; (2)EBSD analysis of the tested specimen to select well oriented grains for deformation (*i.e.,* along ⟨001⟩ orientation); (3) extraction of TEM samples of the selected grains, perpendicular to the ⟨011⟩ grain orientation so the faults are observed edge-on; (4) TEM-EDX analysis of the samples to unveil the operative deformation mechanisms.
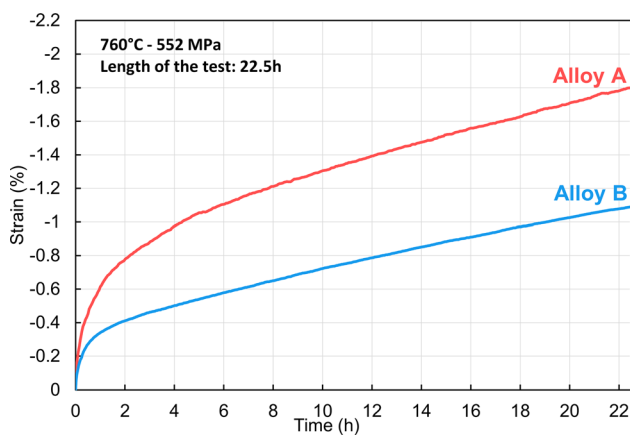

Fig. 4—Experimental creep curves for both Ni-based superalloys tested at 760 °C and 552 MPa. Creep tests were stopped at 22.5 hours.

composition inside the twin recovers the original γ' parent phase composition. As in the previously presented extrinsic fault, Co and Cr are again segregated to the twin boundaries but to a lower extent. This might be a sign of a lower driving force for segregation associated with a lower fault energy for the twin boundary when compared with the previous extrinsic fault. Al is also depleted. In contrast, light segregation of Ta, Nb and Ti can be inferred from the concentration profiles (less conclusive for the case of Nb and Ti).

B. *Faults in Alloy B*

For comparison purposes, the type of faults examined for Alloy B are the same as that for Alloy A (SESF/CESF and microtwin) . However, the population density of microtwins in Alloy B is significantly reduced compare with the extensive population found in Alloy A.
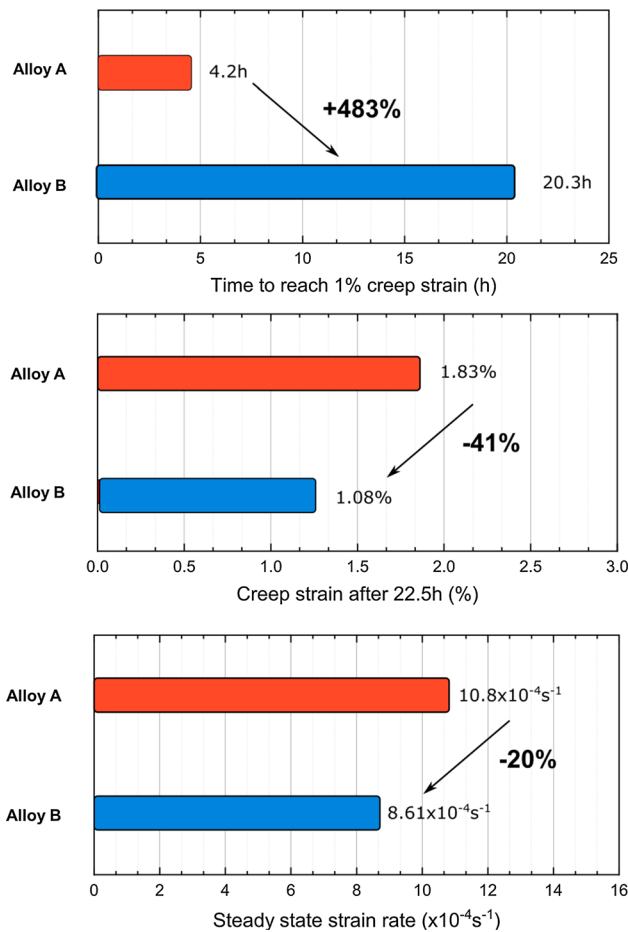
Fig. 5—Top: Time to reach 1 pct creep strain; Middle Creep strain measured at the end of the interrupted tests (after 22.5 hours); Bottom: Creep strain rate of the secondary stage. All data extracted from creep curves.

The combined STEM and EDX analysis of a SESF/CESF found in Alloy B is presented in Figure 9. EDX maps show a strong segregation of Cr at the fault and, at a lower level, segregation of Co. Al depletion can also be inferred. The detailed integrated line scans shown at the bottom of the figure confirm the cited segregation of elements and they also show a modest increase of Ta concentration near the fault line. Specifically remarkable is the increase of Cr at the fault with almost 50 pct higher concentration than the surrounding γ' phase. Another interesting aspect that can be extracted from the line scans is the depletion of segregation elements (*i.e.,* Co and Cr) next to the fault. This fact can also be observed in the EDX map of Cr. On the other hand, it is interesting to observe the opposite phenomena in the case of the Al, solute is piled up next to the Al depleted fault. These segregant depletion and pile up phenomena of Co, Cr and Al next to the faults can be produced presumably by the diffusional fluxes feeding and extracting chemical elements to the fault line's and producing segregation process. This fact would support the previous theories on segregation governed by bulk diffusion[1,24] and reduce the possibility of segregation produced by pipe diffusion supported by other theories.[6,7,8] Further hypotheses of the underlying processes behind this depletion and accumulation phenomena next to the faults are presented in the discussion section.

The STEM and chemical analysis of a microtwin operative in Alloy B is presented in Figure 10. The microtwin is in the early stage of thickening with just 5 layer in thickness. The EDX maps show, similarly to the other faults, segregation of Co and Cr (around 25 pct increase in Cr and 10 pct increase in Co). Nb also presents about a 15 pct increase in composition within the twinned region when compared with the parent γ' phase. Ti fluctuations are not conclusive and within the range of the noise. Due to the reduced thickness of the microtwin (early stage of growth), the segregation is still not split into the twin boundaries but concentrated all along the twin thickness.

C. *Differences in Deformation Mechanisms*

Some preliminary conclusions can be drawn on the deformation mechanisms and segregation phenomena between the two alloys. First, fault growth seems to be promoted by the chemistry of Alloy A (higher concentrations of Co and Cr and lower of Ti, Ta, and Nb within the γ') in comparison with Alloy B. Second, the segregation profiles reveal significant differences: (1) Cr and Co segregation levels in SESFs/CESFs are considerably higher for Alloy A than for Alloy B and (2) Nb segregation is slightly higher for faults observed in Alloy B than in for the ones identified in Alloy A and (3) segregation of Nb seems to be limited mature faults, *e.g.,* microtwins. This last point might indicate that Nb is an element which takes longer times to populate the faults and therefore only appears segregated at microtwins boundaries and not in SESFs/CESFS. No conclusive results were found Ti and Ta segregation. The rationalisation of these findings is discussed in the following section aided by computational simulations of the diffusional processes for both alloys.

IV. DISCUSSION

In this section, focus is put on explaining the connections between compositional changes in the alloy design and the creep performance of the alloy. First, a diffusion-based analytical model is introduced to calculate the fault growth rates for both alloys. Second, these modelling results are used to explain the differences in the creep performance and to propose possible routes in the design of new grades of Ni-based superalloys for mid-temperature and highly stressed components.

A. *Rationalisation of the Chemical Dependency of Creep Performance*

In order to rationalise the observed differences between both studied alloys, a model introduced initially by Barba *et al.*[1] for segregation-assisted fault lengthening is applied here. The cases of SESFs/CESFs and microtwins are studied. The mathematical formulation
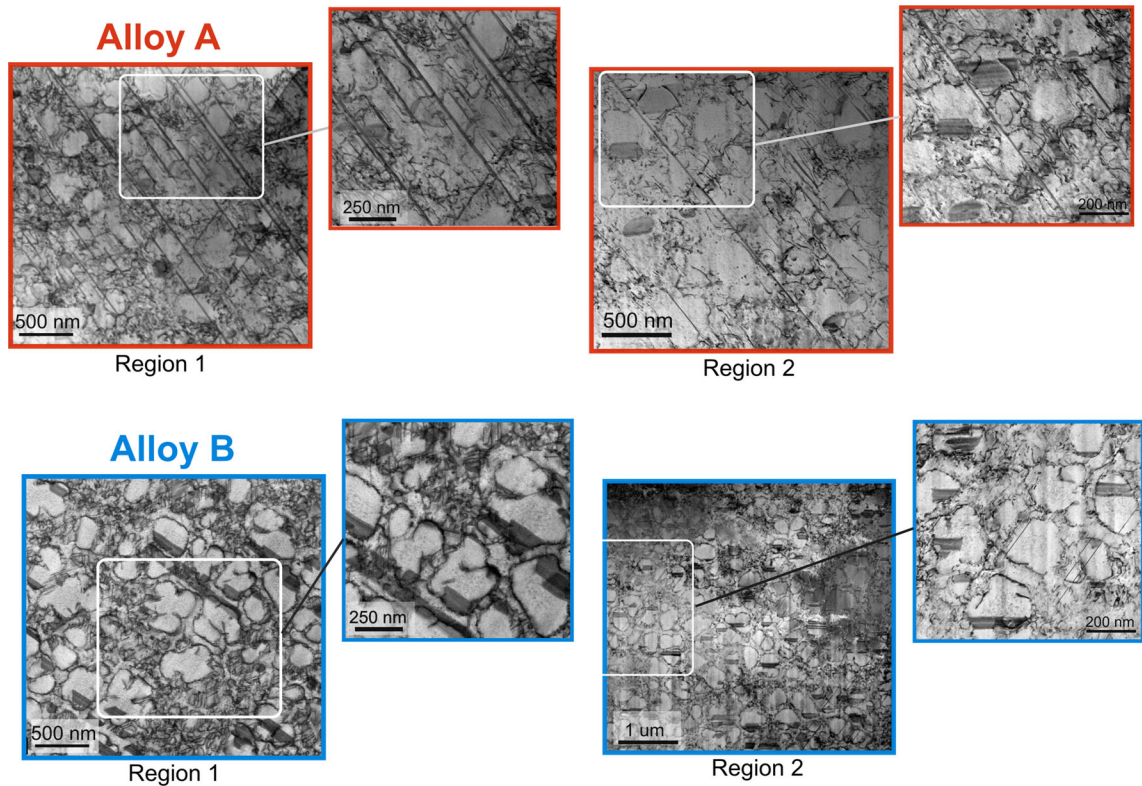
Fig. 6—STEM micrographs of the deformation structures observed for both alloys after testing at 760 °C and 552 MPa. Micrographs are taken from samples extracted from ⟨001⟩ grains oriented perpendicular to ⟨011⟩ crystal orientation. Overall and detailed micrographs are presented for both alloys.

Table III. Estimation of the Twin Population Observed for Both Alloys

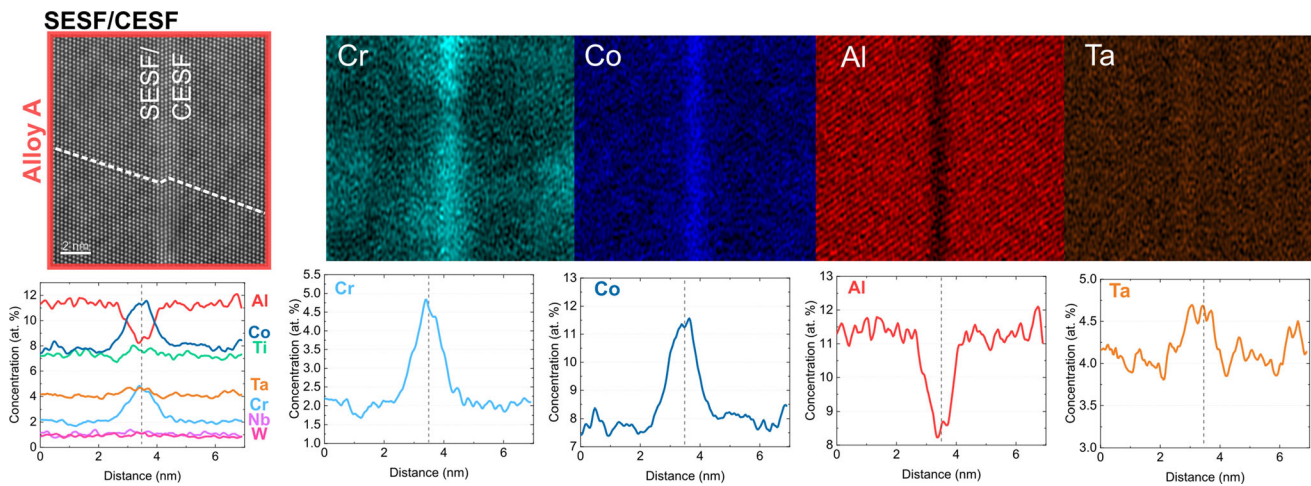|	Alloy A	Alloy B	Ratio Alloy A to Alloy B
Total Twin Length/Area	6.4± 0.7 um/um^2	2.3 ± 0.4 um/um^2	2.8
Average Twin Thickness	12.9 nm	3.1 nm	4.1

Fig. 7—Left: HAADF-STEM detail of a SESF/CESF in Alloy A showing the change of lattice order between the fault and the parent phase. Corresponding integrated EDX horizontal line scans showing the concentration profiles along the fault; Right: detailed EDX integrated line scans showing the segregation of Cr, Co and Ta an the depletion of Al. Dashed lines in EDX line scans indicate reference position of the fault line. Errors estimated for EDX analysis are presented in Appendix A.
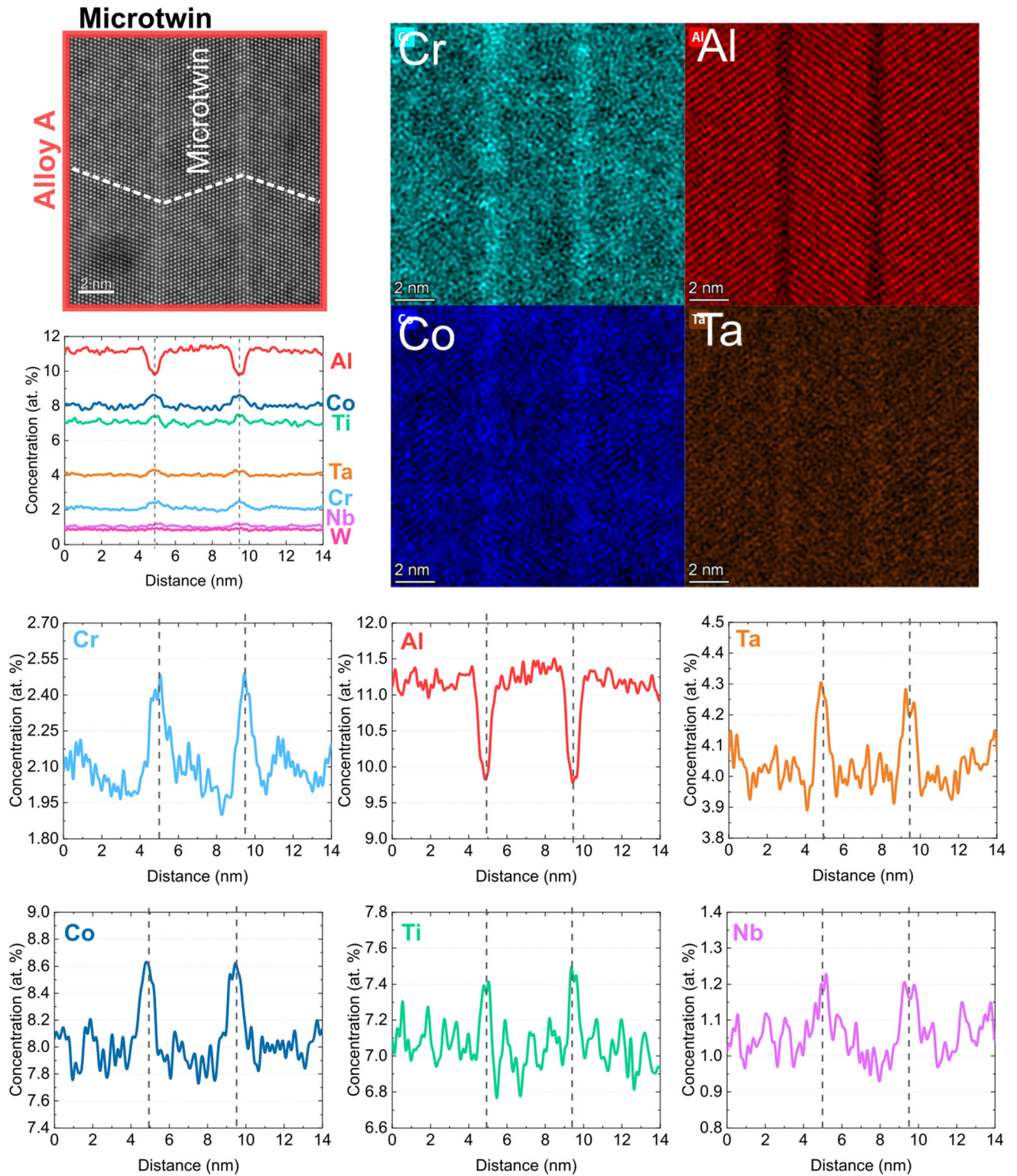
Fig. 8—Top: HAADF-STEM detail of a 23 layer microtwin found in Alloy A showing the change of lattice orientation between the parent and twinned phase, EDS compositional maps and their corresponding horizontal integrated EDX line scans showing the concentration profiles along the microtwin. Right: EDS compositional maps and their integrated EDX horizontal line scan across the twin; Bottom: detailed horizontal EDX line scan across the twin interfaces showing the segregation specially of Cr, Co and Ta and depletion of Al. Dashed lines in EDX line scans indicate reference position of the fault line. Errors estimated for EDX analysis are presented in Appendix A.
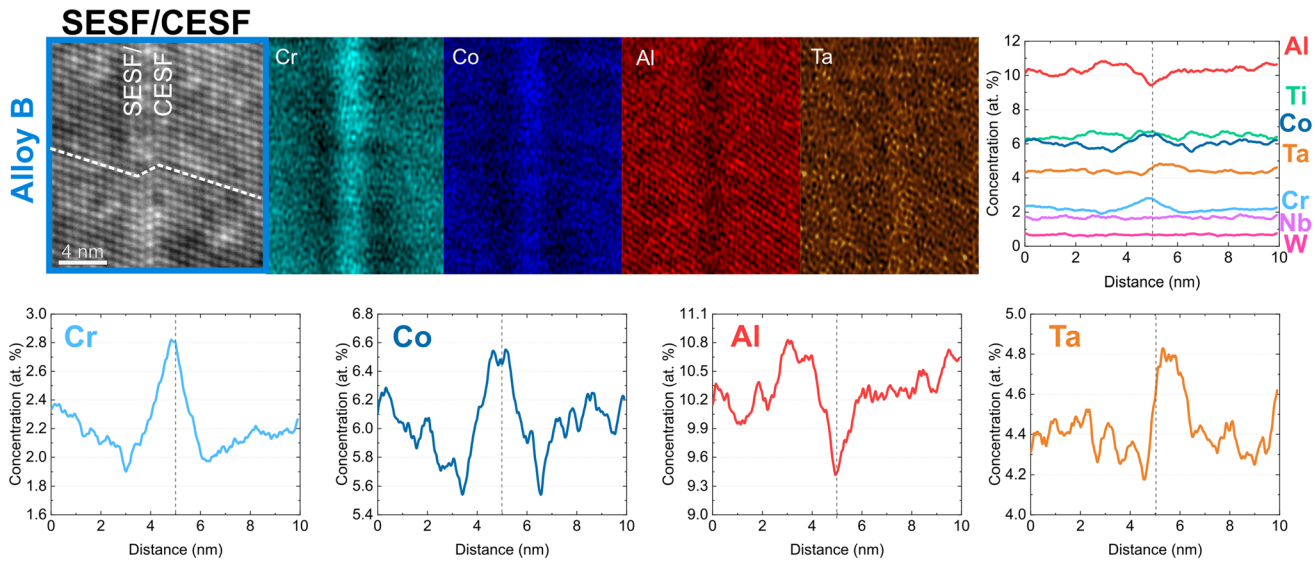
Fig. 9—Top: HAADF micrograph of SESF/CESF formed in Alloy B along with elemental EDX maps and overview integrated chemical horizontal line scans; Bottom: detail of horizontal integrated EDX line scans of segregated or depleted elements at the SESF fault. Dashed lines in EDX line scans indicate reference position of the fault line. Segregation of Cr, Co and Ta in a less extent is observed at the fault line. Errors estimated for EDX analysis are presented in Appendix A.
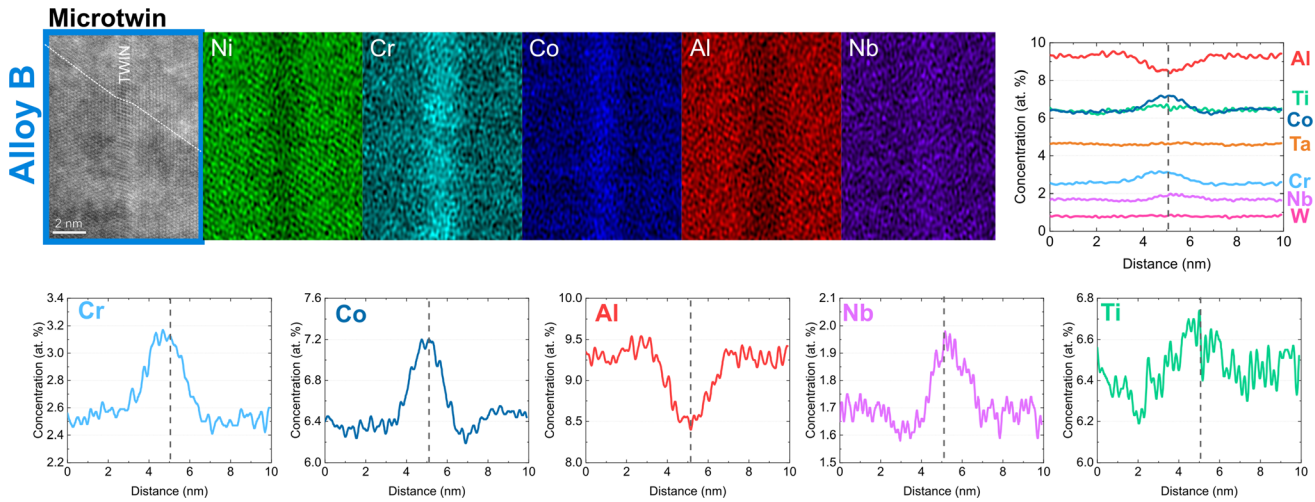

Fig. 10—Top: HAADF micrograph of microtwin found in Alloy B along with elemental EDX maps and overview integrated chemical horizontal line scans; Bottom: detail of horizontal integrated EDX line scans of segregated or depleted elements at the microtwin. Dashed lines in EDX line scans indicate reference position of the fault line. Segregation of Cr, Co and Nb is observed at the fault line. Errors estimated for EDX analysis are presented in Appendix A.

of the model is introduced in Appendix B as a reference. The model is based on solving the diffusion fields around the faults to compute the fault lengthening rates assuming bulk diffusion is feeding the segregation process (conceived as the time-limiting process). A schematic illustration of the lengthening problem is presented in Figure 11.

The lengthening rate of the faults v_f is then computed from the diffusion field by applying the mass conservation law at the growing interface:

$$v_f = D_{eff} \left.\frac{\partial c}{\partial x}\right|_{interface} (c_f - c_p)^{-1}, \qquad [1]$$

where v_f is the fault growth rate, $\left.\frac{\partial c}{\partial x}\right|_{interface}$ is the concentration gradient at the growing interface, $D_{eff} = \frac{\sum_i D_i c_i}{\sum_i c_i}$ is the effective γ' diffusivity of the segregated elements involved in the problem and c_f and c_p are the effective concentrations at the fault and in the parent phase next to the fault tip, respectively. The effective concentrations are defined as $c = \sum_i c_i$. Based on the experimental results, the segregated chemical species included in the diffusion problem are Cr and Co. No conclusive results were obtained for the other alloy elements (e.g., Ti, Nb, W, Zr) and therefore, they are not

included directly in the calculation (although their influence is taken into account by their effect on the diffusivity of Co and Cr). For more details of the mathematical model the reader is referred to the work of Barba et al.[1]

1. Definition of model parameters

In order to assure that the diffusion field recreates the one is operative in real conditions, boundary conditions as effective concentrations at the fault c_f and of the γ' precipitate c_∞ have been computed from the EDX concentration data for each type of fault presented previously. The concentrations at the faults are averaged-integrated assuming the cut-off point to be half of the peak value at the fault. The boundary conditions of equilibrium concentration at the interface c_{eq} is calculated using Thermo-Calc software (database TTNI8) for equilibrium phase calculations, respectively.[18,30] The values for all model concentrations are presented in Table IV.

Additionally, the γ' chemical diffusivities of Co and Cr (D_{Co} and D_{Cr}) are obtained using Thermo-Calc software and DICTRA (database MOBNI3)[30,31] imposing the γ' concentration observed experimentally by EDX. The computed values for the relevant parameters used in the model are detailed in Table IV.

2. Calculated velocities

The lengthening rates computed for the different faults and alloys are presented in Figure 12. For both type of faults (CESFs/SESFs and microtwins) the lengthening rates in Alloy B are lower than in Alloy A. Specifically, 46 pct lower for the case of the SESF/CESF and 37 pct lower for the case of the microtwin. This is in accordance with the creep rates observed experimentally as Alloy A presents higher creep rates and lower performance than Alloy B.

Two subtly different effects might be responsible for what is observed: (1) different diffusion rates within the γ' as the chemistry of this phase changes with alloy composition and (2) different levels of elemental segregation as the driving force for segregation would depend on the γ' composition through the fault energy values. A diffusivity analysis for both alloys is presented in Figure 13 using Thermo-Calc software and DICTRA (database MOBNI3).[30,31] There, three different diffusivities are calculated for the case of the SESF/CESF fault presented in the previous section: (1) an overall average effective diffusivity of all the segregated elements, (2) effective diffusivity of just the principal γ'-stabiliser elements observed in this study (Ti + Ta + Nb) (3) the effective diffusivity of the γ-stabilisers Co and Cr. For all cases, the computed diffusivities are lower for the case of Alloy B. That means that the segregation process, and therefore the fault lengthening process, is retarded by means of the alloy composition. This has implications on alloy design that will be discussed next.

These differences in diffusivites for the two alloys along with the different levels of segregants in the γ' (specially Co and Cr) may also play an important role on the observed depletion and accumulation regions of segregant species next to the fault lines, e.g., Figures 9 and 10. For the case of elements segregating to the fault, it is reasonable to believe that a lower concentration at the γ' and lower diffusivities can promote the formation of depletion areas next to the faults. This is the case as segregants for the fault need to be extracted from smaller regions closer to the fault (due to lower diffusivity) and with low reservoirs of these elements. This is clearly in accordance with these results as Alloy B present a lower diffusivity of these segregation elements (Co and Cr) and also lower amount of them in γ' (specifically for Co), making this alloy more prone to form segregant depleted regions next to the faults (see Figure 9) when compared to Alloy A.

B. Implications to Alloy Design

The diffusivity is dominated by the chemical composition of the alloy. Special focus has been put on this aspect for high-temperature single crystal components (T≥900 °C) by designing alloy compositions with reduced diffusion rates in γ'[32–34] to limit the dislocation climbing. However, for polycrystalline alloys in the mid-range of temperature (T ≈ 500 to 700 °C) the main focus has been historically to increase the shearing strength the γ' force by increasing the stress required to penetrate this phase (specifically by increasing the anti-phase boundary energy and reducing the stacking fault energy to produce partial dissociation). Less focus has been put on limiting the diffusional processes within the γ' when compared with the efforts taken on the high-temperature creep case. However, this work has shown the importance of diffusivities in the γ' is also a critical variable to consider when designing polycrystalline alloys in this mid-temperature range, see Figure 14. Lower diffusivities at the γ' block the segregation processes required for the fault lengthening and thickening in this temperature regime, leading to a reduced amount of creep strain and therefore an improved creep performance.

The data in Figure 14 shows the importance of alloy composition on the elemental diffusivity in the γ'. In general, a 38 pct decrease of diffusivity is achieved from Alloy A to Alloy B (in summary, increasing Ta + Nb levels and decreasing Co + Cr). Similar values are found in the focus is put on the effective diffusivity of Co + Cr (− 27 pct) or Ti + Ta + Nb (− 43 pct). To further confirm this trend in increasing the barrier for elemental diffusion within γ' the activation energies for the diffusion of Co and Cr in the γ' has been calculated in the range of 660 to 860 °C relevant for this study. This was done by Arrhenius fitting of diffusion coefficients calculated every 50 °C. Only Co and Cr were selected as these are the elements were the ones found to strongly segregate to the faults (no conclusive results were found for the segregation of Ta,Ti or Nb by EDX). The estimated activation energies are presented in Table V. There is an increase of 6.9 pct and 4.5 pct in the diffusion activation energy for Co and Cr, respectively. This is translated in higher energy barriers for the segregation to the faults within the γ' for Alloy B when compared
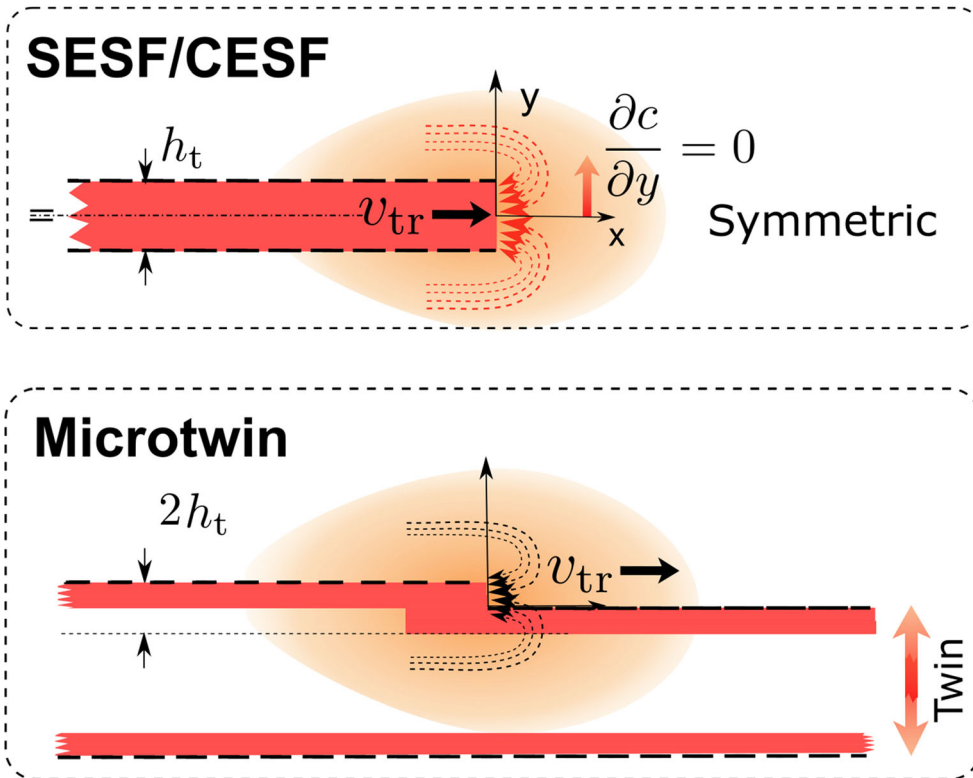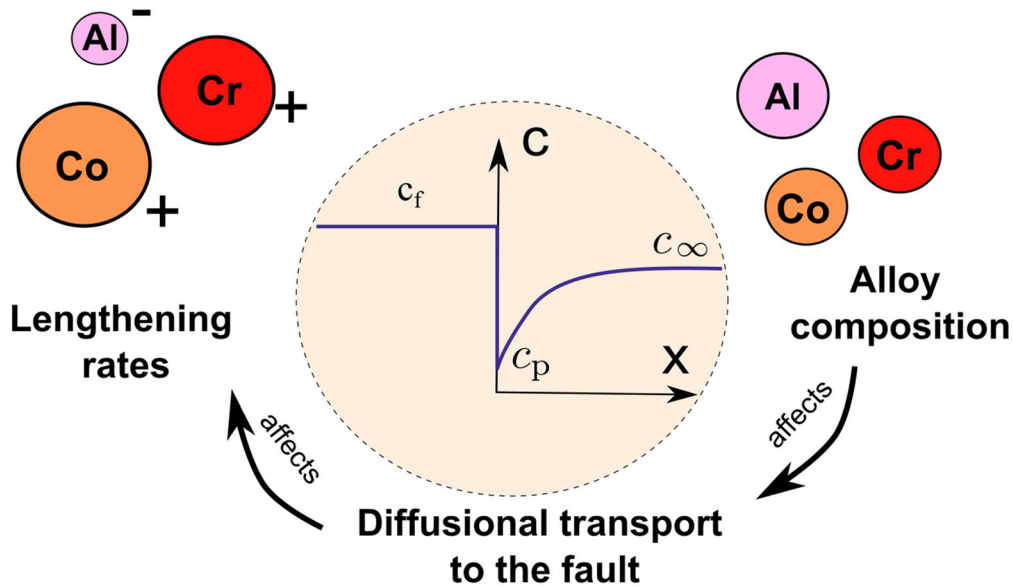
Fig. 11—Diagram of the diffusion problem solved for calculating the lengthening fault rates including detail of schematics of the concentration profile. The model is formulated on the basis of Co and Cr segregation although the effect of the rest of the alloy elements on the diffusivity is accounted for.

with Alloy A. This firmly confirms the trends observed by the Co + Cr diffusivity in Figure 14 and supports the slower lengthening rates observed in this Alloy B when compared to Alloy A.

These results along with the experimental observation emphasize the importance of Ta and Nb additions and Co and Cr subtractions in slowering the fault

segregation process and eventually increasing the creep performance of a polycrystalline superalloy. Although Ti has not been the focus of this article, it is known also to have similar effects to Ta and Nb in blocking the fault lengthening processes.[2,23] In order to quantify the effect of Ti, Ta and Nb on the segregation of Co and Cr, variational calculation of the diffusivities of Co and Cr

Table IV. Averaged Values for the Concentrations of Cr and Co at the Faults (or Fault Interfaces for Microtwins) and at the γ' Precipitates

Alloy	Fault	C_f (at. pct)	C_∞ (at. pct)	C_{eq} (at. pct)	D_{eff} (m^2/s)
Alloy A	SESF/CESF	14.7 pct	10.0 pct	9.9 pct	4.38×10^{-19}
	Twin	10.9 pct	10.3 pct	9.9 pct	2.38×10^{-19}
Alloy B	SESF/CESF	9.2 pct	8.2 pct	8.0 pct	3.08×10^{-19}
	Twin	9.3 pct	8.9 pct	8.0 pct	1.93×10^{-19}

The concentrations at the faults are averaged-integrated assuming the cut-off point to be half of the peak.
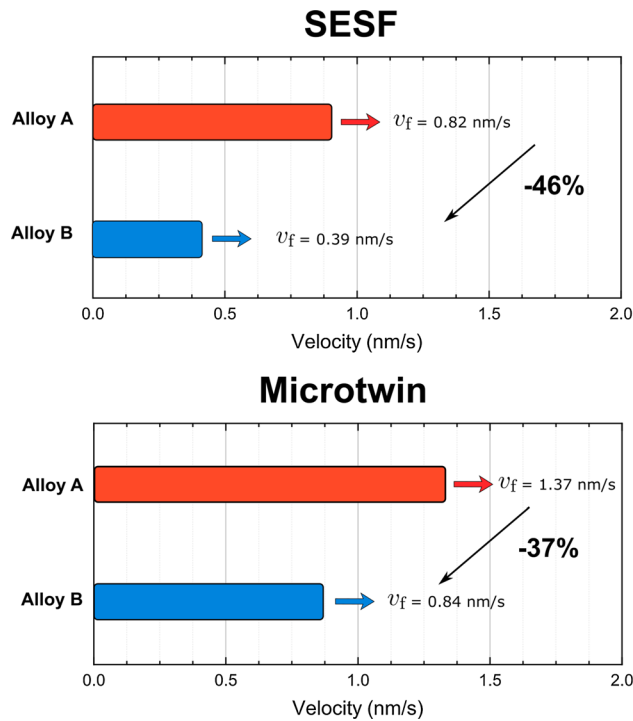

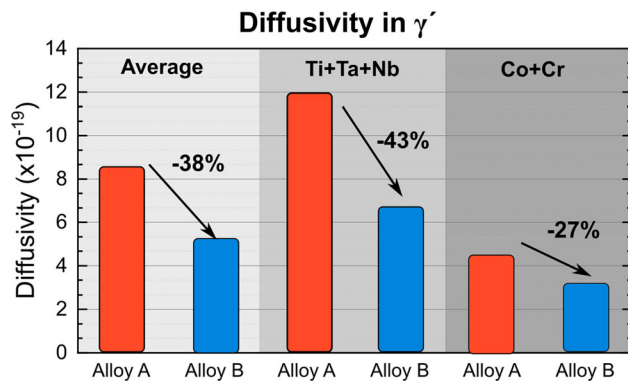Fig. 12—Calculated lengthening rates for SESFs and microtwins as a function of the alloy type.

Fig. 13—Calculated diffusivities in γ' for both alloys. Three cases are presented: (1) effective diffusivity of all elements; (2) effective diffusivity of Ti + Ta + Nb elements and (3) effective diffusivity of Co + Cr elements.

has been performed and the results are presented in Table VI. Based on these results, Ta presents the strongest effect on reducing the mobility of Co and Cr in the γ' followed by Nb. Ti presents a more moderate effect and for Co, it increase its diffusivity. Furthermore, the results suggest that the effect of adding Ta, Nb and Ta is stronger on Cr than on Co. These values, further confirm the effect of Ta and Nb additions on inhibiting the segregation of fault lengthening promoting elements like Co and Cr.

In conclusion, in order to push forward the temperature capabilities of these alloys, these chemistry-dependent diffusional processes need to be fully integrated into future alloy design approaches to capture the dependence of the creep strength of the alloy on its chemical composition.

V. SUMMARY AND CONCLUSIONS

In this work, the creep performance of two different prototype polycrystalline superalloys (Alloys A, B) have been studied. The following specific conclusions can be drawn from this study:

1. Experimental creep testing at 760 °C and 552 MPa shows that the ratio of ordering-promoting elements (Nb-Ti-Ta) to disordering-promoting elements (Co-Cr) strongly affects the creep performance of the alloy. Higher amounts of ordering elements reduce the creep rates considerably improving the creep performance of the alloy ($\dot{\varepsilon}_{AlloyA}^{creep} > \dot{\varepsilon}_{AlloyB}^{creep}$)

2. HR-STEM at atomic resolution has been used to characterize the creep deformation mechanisms of the three alloys and rationalise the reason behind the different creep performance. Alloy A, with higher amount of Co-Cr over Nb-Ta-Ti, present dense population of extensive faults that corresponds to SESFs/CESFs and large fraction of thick twins. Alloy B, with a higher amount of Nb-Ta-Ti and reduced Co-Cr, present a completely different deformation structure: twinning is inhibited and replaced by thin isolated faults (SESFs/CESFs) at the γ'.

3. The chemistry of the faults was studied using atomic resolution EDX. For both alloys, the planar faults examined are enriched with alloy elements different from the parent γ' composition. But coincidences end here: faults in Alloy A present a strong segregation of Co and Cr at the faults and Alloy B also present a marked Nb segregation at the fault plane.
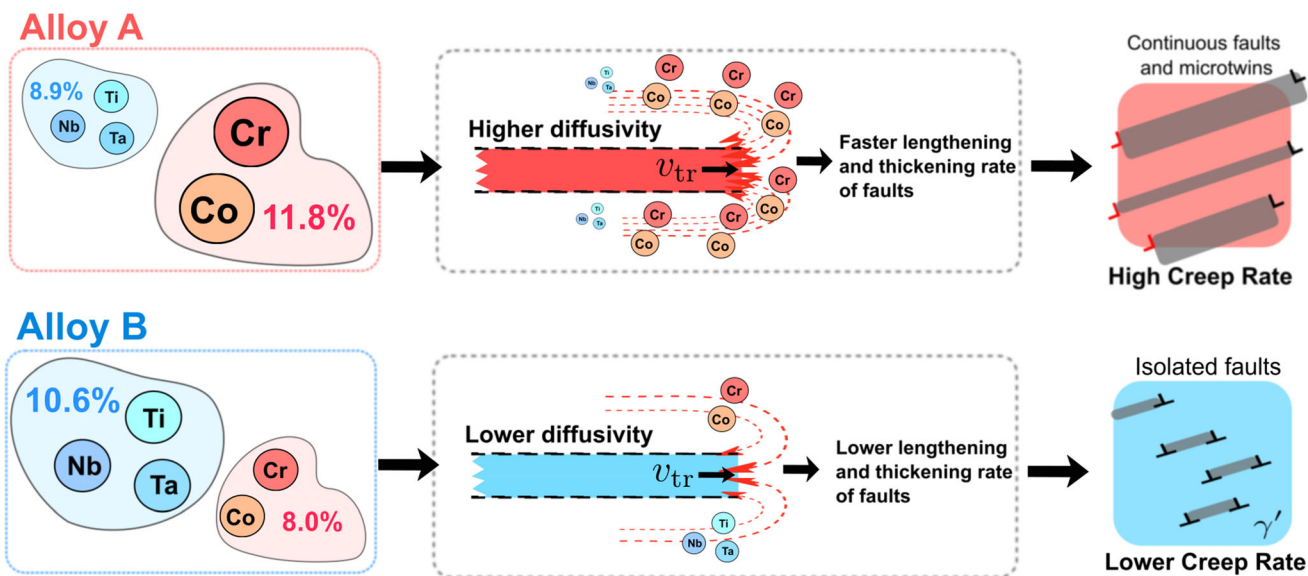
Fig. 14—Diagram of the influence of the alloy composition on the lengthening process of segregation-assisted fault and its connections with the observed operative deformation mechanisms.

Table V. Estimated Activation Energies for Diffusion of Co and Cr in the γ' for Alloy A and Alloy B

	Alloy A	Alloy B	Variation
Q_D^{Co} (kJ/mol)	272	291	+ 6.9 pct
Q_D^{Cr} (kJ/mol)	281	293	+ 4.5 pct

Table VI. Effect of Increasing 1 at. pct of Ti, Ta and Nb in the Diffusivities of Co and Cr in the γ'

	+ 1 at. pct Ti	+ 1 at. pct Ta	+ 1 at. pct Nb
$\triangle D_{Co}^{\gamma'}$	+ 0.9 pct	− 5.3 pct	− 2.3 pct
$\triangle D_{Cr}^{\gamma'}$	− 2.1 pct	− 7.5 pct	− 5.0 pct

Chemical composition of γ' in Alloy A is chosen as baseline composition.

4. The connection between differences in chemical segregants and different creep performance of the three alloys has been rationalised using mathematical modelling of the diffusion lengthening of the faults supported by thermodynamic databases of the γ' structure. The results indicate that alloys with higher amount of order promoting elements (Nb,Ta,Ti) tend to have slower diffusional processes. This inhibits the lengthening and thickening rates of the faults reducing the experimental creep rates in accordance with the experimental results.
5. These new insights on the deformation mechanisms of Ni-based superalloys at mid-temperature regimes and high stresses (T>700 °C and σ>500 MPa) provide a foundation for a new path in the design of creep tolerant polycrystalline superalloys.

CONFLICT OF INTEREST

On behalf of all authors, the corresponding author declares no conflict of interest.

APPENDIX A: ESTIMATION OF ERRORS IN EDX ANALYSIS

In this Appendix, the errors estimated for the chemical analysis performed on the faults is presented. For each fault, the region of interest (ROI) to estimate the error has been set as the area used to integrate the compositional line scans (Tables VII, VIII, IX and X).

APPENDIX B: PHASE TRANSFORMATION DIFFUSION PROBLEM

The mathematical model proposed by Barba et al.[1] for the case of Co and Cr partitioning controlled growth of microtwins is adapted here. A schematic diagram of the physical problem is shown in Figure 8(a). The boundary condition that governs the ledge growth is obtained from the mass conservation at the interface:

Table VII. Estimated Error in Chemical Measurements Provided by TEM-EDX in the ROI of the Microtwin Analysed in Alloy A in Fig. 8

		Alloy A Microtwin EDX Error in ROI	
Element	Family	Atomic fraction (percent)	Atomic error (percent)
Al	K	14.52	1.43
Ti	K	6.96	1.29
Cr	K	1.62	0.27
Co	K	7.83	1.23
Ni	K	66.32	3.45
Nb	K	0.68	0.11
Ta	L	1.37	0.20
W	L	0.69	0.10

Table VIII. Estimated Error in Chemical Measurements Provided by TEM-EDX in the ROI of the SESF/CESFF Analysed in Alloy A in Fig. 7

		Alloy A SESF/CESF EDX Error in ROI	
Element	Family	Atomic fraction (percent)	Atomic error (percent)
Al	K	14.38	1.42
Ti	K	7.22	1.33
Cr	K	2.08	0.34
Co	K	8.31	1.30
Ni	K	65.72	3.49
Nb	K	0.64	0.10
Ta	L	1.16	0.17
W	L	0.49	0.07

Table IX. Estimated Error in Chemical Measurements Provided by TEM-EDX in the ROI of the Microtwin Analysed in alloy B in Fig. 10

		Alloy B Microtwin EDX Error in ROI	
Element	Family	Atomic fraction (percent)	Atomic error (percent)
Al	K	12.13	1.24
Ti	K	6.39	1.20
Cr	K	2.28	0.38
Co	K	6.45	1.04
Ni	K	68.78	3.31
Nb	K	1.29	0.21
Ta	L	2.00	0.29
W	L	0.68	0.10

Table X. Estimated Error in Chemical Measurements Provided by TEM-EDX in the ROI of the SESF/CESFF Analysed in Alloy B in Fig. 9

		Alloy B Microtwin EDX Error in ROI	
Element	Family	Atomic fraction (percent)	Atomic error (percent)
Al	K	13.21	1.34
Ti	K	6.43	1.21
Cr	K	1.86	0.31
Co	K	5.99	0.96
Ni	K	68.52	3.31
Nb	K	1.30	0.21
Ta	L	2.00	0.29
W	L	0.68	0.10

$$v_{\mathrm{f}} = D_{\mathrm{eff}} \left.\frac{\partial c}{\partial X}\right|_{step} (c_{\mathrm{f}} - c_{\mathrm{p}}), \qquad [\mathrm{A1}]$$

where v_{f} is the microtwin ledge velocity, X is the absolute coordinate along the twin length, $D_{\mathrm{eff}} = \frac{D_{\mathrm{Co}} c_{\mathrm{Co}} + D_{\mathrm{Cr}} c_{\mathrm{Cr}}}{c_{\mathrm{Co}} + c_{\mathrm{Cr}}}$ is the effective diffusivity of Co and Cr in the parent phase and c_{f} and c_{p} are the effective Co + Cr concentrations in the twin phase and in the parent phase at the twin step, respectively.

The diffusion in the parent phase around the twin is governed by Fick's laws,[35] and for simplicity, the twin phase is assumed to be non-diffusive. The diffusion problem is formulated in a moving non-dimensional coordinate system $x = (X - v_{\mathrm{f}})/h$ and $y = Y/h$ (relative to global coordinates $X - Y$). Introducing the Péclet number $p = v_{\mathrm{f}} h / 2 D_{\mathrm{eff}}$, the problem is defined by

$$\begin{cases} \nabla^2 \Gamma(x,y) + 2p\frac{\partial \Gamma}{\partial x} = 0 \\ \frac{\partial \Gamma}{\partial y} = 0 \quad \text{for } y = 1, \ x < 0 \\ \frac{\partial \Gamma}{\partial y} = 0 \quad \text{for } y = 0, \ x > 0 \\ \frac{\partial \Gamma}{\partial x} = -\alpha^{-1}(p) \quad \text{for } x = 0, \ 0 \le y < 1 \end{cases}, \qquad [\mathrm{A2}]$$

where $\alpha(p)$ is a function to be determined and the dimensionless concentration is defined by

$$\Gamma(x,y) = \frac{c(x,y) - c_{\infty}}{c_{\mathrm{e}} - c_{\infty}}, \qquad [\mathrm{A3}]$$

where c_{e} is the equilibrium Co + Cr concentration at the interface. We include the effect of the interface reactions (short-range reordering) on the twin kinetics by considering deviation from the equilibrium at the interface ($c_{\mathrm{p}} \ne c_{\mathrm{e}}$). For this case, the extra-boundary condition needed is imposed by accounting for the mobility μ_0, which is controlled by short-range atomic reshuffling:

$$v_{\mathrm{t}} = \mu_0 (c_{\mathrm{p}} - c_{\mathrm{e}}) \qquad [\mathrm{A4}]$$

In case of large μ_0 the problem is diffusion-controlled ($\mu_0 \to \infty$ implies $c_{\mathrm{p}} \to c_{\mathrm{e}}$), whereas for small μ_0 the problem is reaction-controlled. A non-dimensional interface mobility is introduced in the interface analysis:

$q = \mu_0 (c_{\mathrm{f}} - c_{\mathrm{e}})(4D/h)^{-1}$. The estimation of the interface mobility for this problem is addressed in Barba et al.[1] For this problem the lengthening has been shown to be diffusion-controlled and therefore, there can be assumed to be not relevant influence of the interface reactions on the lengthening kinetics.

The approximated solution using Fourier transforms and perturbation theory proposed by Trivedi and Jones[36] and Atkinson[37] leads to a set of two non-linear equations for $0.003 \le p < 0.500$:

$$\begin{cases} [\alpha(p)]^{-1} = p + \sum_{i=0}^{7} k_i [\log_{10}(p)]^i \\ \Omega_0 = 2p\alpha(p) + (p/q)(1 - 2p\alpha(p)) \end{cases}, \qquad [\mathrm{A5}]$$

where $k_0 = 1.68262$, $k_1 = 2.84725$, $k_2 = 5.58040$, $k_3 = 7.19946$, $k_4 = 5.49601$, $k_5 = 2.41352$, $k_6 = 0.55658$ and $k_7 = 0.05182$ and $q = \mu_0 (c_{\mathrm{f}} - c_{\mathrm{e}})(4D_{\mathrm{eff}}/h)^{-1}$ is the non-dimensional interface mobility (μ_0 is the interface mobility). In this system, $\alpha(p)$ and p are the unknowns to obtain and Ω_0 is defined as the dimensionless normalized supersaturation concentration $c_0 = (c_{\infty} - c_{\mathrm{e}})/(c_{\mathrm{f}} - c_{\mathrm{e}})$. Once this system is solved, the velocity of the twin ledge can be recovered from the definition of Péclet number. This process allows for the estimation of the microtwin lengthening rate v_{f}.

REFERENCES

1. D. Barba, D. Pedrazzini, A. Collins, A.J. Wilkinson, M.P. Moody, P.A.J. Bagot, A. Jérusalem, and R.C. Reed: *Acta Mater.*, 2017, vol. 127, pp. 37–40.
2. A.J. Egan, Y. Rao, G.B. Viswanathan, T.M. Smith, M. Ghazisaeidi, S. Tin, and M.J. Mills: in *Superalloys 2020*, Springer, Cham, 2020, pp. 640–50. https://link.springer.com/chapter/10.1007/978-3-030-518 34-9_62.
3. Y.M. Eggeler, J. Müller, M.S. Titus, A. Suzuki, T.M. Pollock, and E. Spiecker: *Acta Mater.*, 2016, vol. 113, pp. 35–349.
4. L.P. Freund, O.M. Messé, J.S. Barnard, M. Göken, S. Neumeier, and C.M. Rae, *Acta Mater.*, 2017, vol. 123, pp. 295–304.
5. P. Kontis: *Scripta Mater.*, 2021, vol. 194, p. 113626.
6. P. Kontis, Z. Li, D.M. Collins, J. Cormier, D. Raabe, and B. Gault: *Scripta Mater.*, 2018, vol. 145, pp. 76–80.
7. L. Lilensten, S. Antonov, B. Gault, S. Tin, and P. Kontis: *Acta Mater.*, 2021, vol. 202, pp. 232–42.
8. S.K. Makineni, A. Kumar, M. Lenz, P. Kontis, T. Meiners, C. Zenk, S. Zaefferer, G. Eggeler, S. Neumeier, E. Spiecker, D.

Raabe, and B. Gault: *Acta Mater.*, 2018, vol. 155, pp. 362–71. https://doi.org/10.1016/j.actamat.2018.05.074.

9. T. Smith, Y. Rao, Y. Wang, M. Ghazisaeidi, and M. Mills: *Acta Mater.*, 2017, vol. 141, pp. 261–72.
10. R.C. Reed: *The Superalloys: Fundamentals and Applications.* Cambridge University Press, 2008. https://www.cambridge.org/core/books/superalloys/00CEE7E1026FA82BBC9F335E75D57AB2.
11. R.C. Reed and C.M.F. Rae: in *Physical Metallurgy*, 5th ed., D.E. Laughlin and K. Hono, eds., Elsevier, 2014, pp. 2215–90. https://www.sciencedirect.com/science/article/pii/B9780444537706000228.
12. D. Barba, T. Smith, J. Miao, M. Mills, and R. Reed: *Metall. Mater. Trans. A*, 2018, vol. 49(9), pp. 4173–85.
13. A.J. Egan, F. Xue, Y. Rao, G. Sparks, E. Marquis, M. Ghazisaeidi, S. Tin, and M.J. Mills: *Acta Mater.*, 2022, vol. 238, p. 118206.
14. Y. Eggeler, K. Vamsi, and T. Pollock: *Annu. Rev. Mater. Res.*, 2021, vol. 51(1), pp. 209–40.
15. L. Feng, Y. Rao, M. Ghazisaeidi, M.J. Mills, and Y. Wang: *Acta Mater.*, 2020, vol. 200, pp. 223–35.
16. S. Lu, S. Antonov, F. Xue, L. Li, and Q. Feng: *Acta Mater.*, 2021, vol. 215, p. 117099.
17. S. Shang, C. Zacherl, H. Fang, Y. Wang, Y. Du, and Z. Liu: *J. Phys.: Condens. Matter.*, 2012, vol. 24(50), p. 505403.
18. D. Wen and M.S. Titus: *Acta Mater.*, 2021, vol. 221, p. 117358.
19. D. Barba, S. Pedrazzini, A. Vilalta-Clemente, A.J. Wilkinson, M.P. Moody, P.A.J. Bagot, A. Jérusalem, and R.C. Reed: *Scripta Mater.*, 2017, vol. 127, pp. 37–40.
20. L. Kovarik, R.R. Unocic, J. Li, P. Sarosi, C. Shen, Y. Wang, and M.J. Mills: *Progress Mater. Sci.*, 2009, vol. 54, pp. 839–73.
21. J.J. Moverare, S. Johansson, and R.C. Reed: *Acta Mater.*, 2009, vol. 57(7), pp. 2266–76.
22. D. Barba, A.J. Egan, Y. Gong, M.J. Mills, and R.C. Reed: in *Superalloys 2020*, Springer, Cham, 2020, pp. 260–72. https://link.springer.com/chapter/10.1007/978-3-030-51834-9_25.
23. T.M. Smith, T.P. Gabb, K.N. Wertz, J. Stuckner, L.J. Evans, A.J. Egan, and M.J. Mills: in *Superalloys 2020*, Springer, Cham, 2020, pp. 726–36. https://link.springer.com/chapter/10.1007/978-3-030-51834-9_70.
24. T.M. Smith, B.D. Esser, N. Antolin, A. Carlsson, R.E.A. Williams, A. Wessman, T. Hanlon, H.L. Fraser, W. Windl, D.W. McComb, and M.J. Mills: *Nat. Commun.*, 2016, vol. 7, p. 13434.
25. L. Feng, D. Lv, R. Rhein, J. Goiri, M. Titus, A. Van der Ven, T. Pollock, and Y. Wang: *Acta Mater.*, 2018, vol. 161, pp. 99–109.
26. Y. Rao, T. Smith, M. Mills, and M. Ghazisaeidi: *Acta Mater.*, 2018, vol. 148, pp. 173–84.
27. H. Hisazawa, Y. Terada, F. Adziman, D.J. Crudden, D.M. Collins, D.E. Armstrong, and R.C. Reed: *Metals*, 2017, vol. 7(3), p. 71.
28. T.M. Smith, R.R. Unocic, H. Deutchman, and M.J. Mills: *Mater. High Temp.*, 2016, vol. 33(33), pp. 1–12.
29. H. Hoeft and P. Schwaab: *X-Ray Spectrom.*, 1988, vol. 17(5), pp. 201–8.
30. J.O. Andersson, T. Helander, L. Höglund, P. Shi, and B. Sundman: *Calphad*, 2002, vol. 26(2), pp. 273–312.
31. Thermotech Ni-based Superalloys Database v8.0. Accessed Jan 2015.
32. J.-B. Le Graverend, J. Cormier, S. Kruch, F. Gallerneau, and J. Mendez: *Metall. Mater. Trans. A*, 2012, vol. 43(11), pp. 3988–97.
33. C. Rae and R. Reed: *Acta Mater.*, 2007, vol. 55(3), pp. 1067–81.
34. Z. Zhu, H. Basoalto, N. Warnken, and R.C. Reed: *Acta Mater.*, 2012, vol. 60(12), pp. 4888–900.
35. A. Fick: The London. *Edinb. Dublin Philos. Mag. J Sci.*, 1855, vol. 10, pp. 30–9.
36. G.J. Jones and R.K. Trivedi: *J. Appl. Phys.*, 1971, vol. 42(11), pp. 4299–304.
37. C. Atkinson: *Proceedings of the Royal Society of London*, Springer, Cham, 1981, pp.351–68.